The Astrophysical Journal, 598:1277–1289, 2003 December 1

MODELING THE Ne IX TRIPLET SPECTRAL REGION OF CAPELLA WITH THE *CHANDRA* AND *XMM-NEWTON* GRATINGS

Jan-Uwe Ness
Hamburger Sternwarte, Universität Hamburg, Gojenbergsweg 112, D-21029 Hamburg, Germany;
jness@hs.uni-hamburg.de

Nancy S. Brickhouse and Jeremy J. Drake
Harvard-Smithsonian Center for Astrophysics, 60 Garden Street, Cambridge, MA 02138;
bhouse@head-cfa.harvard.edu, jdrake@head-cfa.harvard.edu

and

David P. Huenemoerder
MIT Center for Space Research, 70 Vassar Street, Cambridge, MA 02139;
dph@space.mit.edu
Received 2003 March 7; accepted 2003 August 6

ABSTRACT

High-resolution X-ray spectroscopy with the diffraction gratings of *Chandra* and *XMM-Newton* offers new chances to study a large variety of stellar coronal phenomena. A popular X-ray calibration target is Capella, which has been observed with all gratings with significant exposure times. We gathered together all available data of the High Energy Transmission Grating Spectrometer (HETGS; 155 ks), Low Energy Transmission Grating Spectrometer (LETGS; 219 ks), and Reflection Grating Spectrometer (RGS; 53 ks) for comparative analysis, focusing on the Ne IX triplet at around 13.5 Å, a region that is severely blended by strong iron lines. We identify 18 emission lines in this region of the High-Energy Grating (HEG) spectrum, including many from Fe XIX, and find good agreement with predictions from a theoretical model constructed using the Astrophysical Plasma Emission Code. The model uses an emission measure distribution derived from Fe XV to Fe XXIV lines. The success of the model is due in part to the inclusion of accurate wavelengths from laboratory measurements. While these 18 emission lines cannot be isolated in the LETGS or RGS spectra, their wavelengths and fluxes as measured with HEG are consistent with the lower resolution spectra. In the Capella model for HEG, the weak intercombination line of Ne IX is significantly blended by iron lines, which contribute about half the flux. After accounting for blending in the He-like diagnostic lines, we find the density to be consistent with the low-density limit ($n_e < 2 \times 10^{10}$ cm^{-3}); however, the electron temperature indicated by the Ne IX *G*-ratio is surprisingly low ($\sim$2 MK) compared to the peak of the emission measure distribution ($\sim$6 MK). Models show that the Ne IX triplet is less blended in cooler plasmas and in plasmas with an enhanced neon-to-iron abundance ratio.

Subject headings: atomic data — line: identification — stars: coronae — stars: individual (Capella) — stars: late-type — X-rays: stars

1. INTRODUCTION

Investigation of stellar coronae in the X-ray wavelength band has until very recently been restricted to instruments with intrinsically low spectral resolution, such as the proportional counters and CCDs on satellites such as *Einstein*, *ROSAT*, *ASCA*, and *BeppoSAX*.[1] The limitations of low-resolution spectra have restricted X-ray studies of stellar coronae to measurements of luminosities and plasma temperatures and estimates of elemental abundances. The spatial resolution of X-ray–emitting plasma that is routinely available for studies of the solar corona with satellites such as the *Solar and Heliospheric Observatory* and *TRACE* is still today a dream for stellar X-ray astronomers.

Despite limited spectral information, substantial progress has been made in understanding the gross characteristics of stellar coronae throughout the H-R diagram. For example, Schrijver, Mewe, & Walter (1984) showed from *Einstein* Imaging Proportional Counter observations of a sample of 34 late-type stars that coronal temperature was directly correlated with X-ray luminosity and stellar rotation rate. Similar results were obtained for a larger sample by Schmitt et al. (1990) and later based on the so-called hardness ratio obtained from *ROSAT* PSPC observations by Schmitt (1997).

These results raised a question as to the nature of the high-temperature plasma in active stellar coronae. Vaiana & Rosner (1978) had pointed out that the Sun completely covered with active regions would have an X-ray luminosity of $\sim 2 \times 10^{29}$ ergs s^{-1}. However, the most active solar-like stars can have X-ray luminosities up to 2 orders of magnitude higher than this and so cannot simply be scaled-up versions of the solar corona. The hot plasma on the most active stars must be structured differently from that in typical solar active regions. The radiative loss of a hot, optically thin, collision-dominated plasma is essentially proportional to the volume emission measure, defined as the product of electron density squared and the emitting volume, $n_e^2 V$. Increasing either the emitting volumes or plasma density results in an increase in X-ray luminosity.

[1] Exceptions are the *Einstein* spectra of Capella with much better resolution, obtained by Mewe et al. (1982) with the Objective Grating Spectrometer, covering the range 5–30 Å with a resolution of less than 1 Å, and of Vedder & Canizares (1983) with the Focal Plane Crystal Spectrometer.

A key plasma parameter for inferring the size of X-ray–emitting regions is therefore the plasma density. Direct spectroscopic information on plasma densities at coronal temperatures on stars other than the Sun first became possible with the advent of "high-resolution" spectra ($\lambda/\Delta\lambda \sim 200$) obtained by the *Extreme Ultraviolet Explorer* (*EUVE*) that were capable of separating individual spectral lines. Even with this resolution, the available diagnostics have often tended to be less than definitive, owing to the poor signal-to-noise ratio of observed spectra or to blended lines. This has been especially the case for active stars. Studies of density-sensitive lines of Fe XIX to Fe XXII in *EUVE* spectra of RS CVn stars revealed tempting evidence for high densities of $n_e \sim 10^{12}$–10^{13} cm^{-3} at coronal temperatures near 10^7 K (Dupree et al. 1993; Drake 1996). Such high densities suggest that emitting structures are compact: static loop models such as those described by Rosner, Tucker, & Vaiana (1978) would have heights of ~1000 km with confining field strengths of up to 1 kG and surface filling factors of 1%–10%. In the case of the evolved active binary Capella, Brickhouse (1996) obtained $n_e \sim 10^{12}$ cm^{-3} from Fe XIX to Fe XXII but $n_e \sim 10^9$ cm^{-3} based on Fe XII to Fe XIV, suggesting that the cool and hot plasma are from distinctly different structures. In contrast to the high densities reported by Dupree et al. (1993), only upper limits were found by Mewe et al. (2001) [$n_e < (2\text{–}5) \times 10^{12}$ cm^{-3}] using the same line ratios of Fe XX to Fe XXII but with the higher spectral resolution of the *Chandra* LETGS spectra. They point out that the Fe XIX to Fe XXII line ratios are only sensitive above 10^{11} cm^{-3}, such that no tracer for low densities for the hotter plasma component is available.

The high spectral resolution of *Chandra* and *XMM-Newton* has significantly changed the situation regarding plasma diagnostics for stellar coronae. High spectral resolution coupled with large effective area allows the application of line-based diagnostic techniques at X-ray wavelengths. Line ratios of the strong H-like Lyman series, which are sensitive to the Boltzmann factor, and the He-like triplets, which exploit the competition between collisional excitation and recombination-driven cascades, can be useful temperature diagnostics. Simply examining the presence or absence of principle lines of different ionic states of different elements gives an indication of the emitting plasma temperatures. The He-like systems also provide density diagnostics based on the low-lying metastable level $1s2s\,^3S_1$ above the $1s^2\,^1S_0$ ground state. The He-like oxygen diagnostic has been used to support the previous *EUVE* result for Capella, showing that the lower temperature plasma (~2 MK) also has lower density (Canizares et al. 2000; Brinkman et al. 2000; Ness et al. 2001; Audard et al. 2001; Brickhouse 2002).

We compare the capabilities of this current generation of high spectral resolution X-ray instruments with a detailed study of the Ne IX triplet as a density and temperature diagnostic. We focus our study on the Capella binary system (HD 34029; α Aurigae; G8 III + G1 III). Capella has been extensively studied from X-ray to radio wavelengths and is the brightest steady coronal source in the X-ray sky. As such, it has been a key calibration target for the *Chandra* high-energy and low-energy transmission grating spectrometers (HETGS and LETGS, respectively), as well as the *XMM-Newton* reflection grating spectrometers (RGS1 and RGS2), and has been observed on several occasions by both satellites (Canizares et al. 2000; Brinkman et al. 2000; Audard et al. 2001). The emission measure distribution of Capella shows a steep but narrow enhancement at 6 MK (Dupree et al. 1993; Brickhouse et al. 2000), making it ideal for studying the blending of Ne IX with high-temperature lines.

The purpose of this study is threefold: (1) to assess the accuracy and reliability of state-of-the-art plasma radiative loss models for describing the emission spectrum of Capella in the region of the He-like complex of Ne, (2) to determine how well these models might describe the spectra of stars both more and less active than Capella and with different coronal temperatures, and (3) to gain further insight into the plasma density in the Capella coronae in the key temperature range of 4–6 MK.

2. He-LIKE IONS IN HIGH-RESOLUTION STELLAR SPECTRA

2.1. *The Use of the* He-*like Triplet Diagnostics*

He-like ions are produced at temperatures ranging between ~2 MK for C V and N VI and 10 MK for Si XIII. The densities over which the diagnostics are sensitive increase with increasing element number Z, such that the lower Z ions C V, N VI, and O VII, with temperatures of peak emissivity at 1.0, 1.6, and 2.0 MK, respectively, provide diagnostics for densities up to ~10^{12} cm^{-3}. The higher temperature (>6 MK) ions Mg XI and Si XIII are sensitive at densities above ~10^{12} cm^{-3}. Ne IX, typically formed at ~4 MK, is sensitive to densities between ~10^{11} and 10^{13} cm^{-3}. In many cases measurements of Ne IX are the only chance to fill the gap between the cooler plasma and the hotter plasma. In addition, some stars show a neon overabundance (e.g., Brinkman et al. 2001; Drake et al. 2001; Güdel et al. 2001; Huenemoerder, Canizares, & Schulz 2001), making Ne IX lines more easily detectable in those cases. However, blending with Fe lines in the Ne IX triplet spectral region can compromise the diagnostic utility when analyzing plasmas hot enough to produce them (especially Fe XIX at ~6 MK).

The theory of the He-like triplets was originally developed by Gabriel & Jordan (1969). The density diagnostic is often referred to as the R-ratio, where $R = f/i$, denoting the forbidden line flux with f and the intercombination line flux with i. The relation can be parameterized as

$$R = \frac{R_0}{1 + n_e/N_c} , \tag{1}$$

with low-density limit R_0 and electron density n_e. The critical density N_c is the density at which $R = 1/2R_0$. Pradhan & Shull (1981) and Blumenthal, Drake, & Tucker (1972) calculated theoretical values of R_0 and N_c and determined the Z-dependence of the density sensitivity as shown in Figure 1. Larger R-ratios mean relatively weaker intercombination lines; since the i is intrinsically weak at low densities, it may be difficult to measure accurately.

Strong ultraviolet radiation fields can also depopulate the metastable levels of the He-like triplets and change the R-ratios. For the case of Capella and Ne IX, such fields can be neglected (Ness et al. 2001).

For an optically thin plasma, a temperature diagnostic is

$$G = \frac{i + f}{r} , \tag{2}$$

where r is the resonance line flux. In collisional ionization

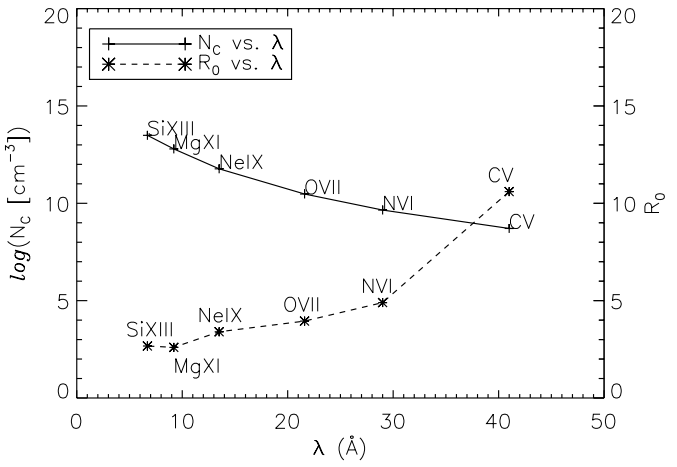

FIG. 1.—Low-density limits R_0 and critical densities N_c for the different He-like ions showing systematic, anticorrelated trends with wavelength, due ultimately to the nuclear charge (from Pradhan & Shull 1981; Blumenthal et al. 1972). Large R_0 (C V) implies that the i flux may be difficult to measure. Large N_c may be outside the interesting coronal range (Si XIII). Ne IX appears to have ideal values for coronal physics.

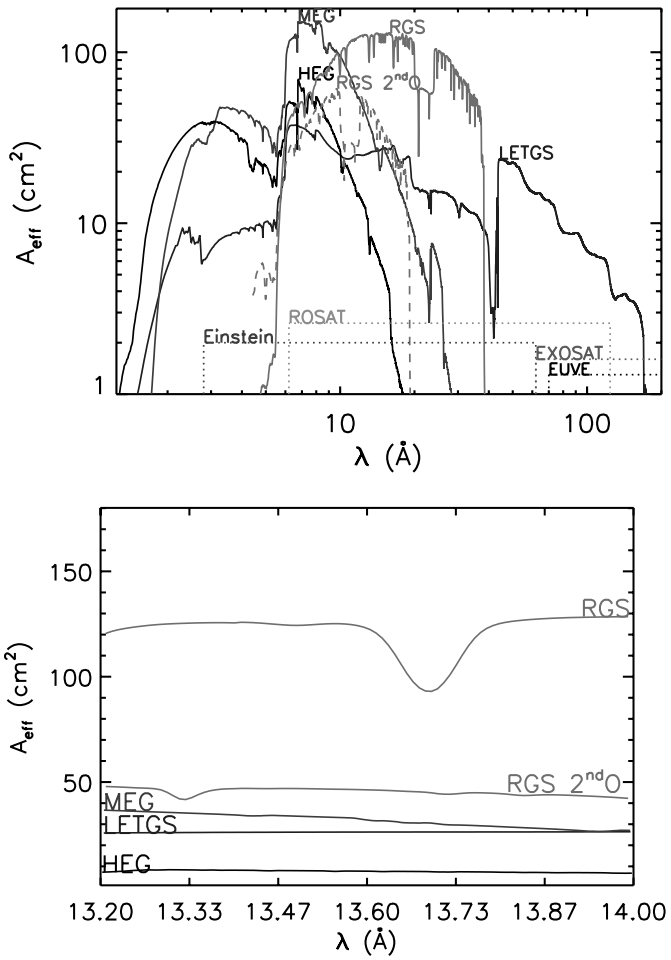

FIG. 2.—Effective areas for the *Chandra* and *XMM-Newton* gratings, with ranges of other observatories shown as dotted lines. At 13.6 Å, the RGS has the largest area, while HEG is the least sensitive. The bottom panel shows detail in the Ne IX region.

equilibrium (CIE), the G-ratio decreases with temperature primarily because the excitation of the triplet levels (by dielectronic recombination-driven cascades) decreases faster than the collisional excitation to the $^1P_1$ (see Smith et al. 2001). Assuming a priori that the plasma is in CIE, the G-ratio is a direct diagnostic of the temperature of Ne IX emission and can be compared with predictions based on an emission measure distribution.

The He-like triplets have been used for measuring temperatures and densities in the solar corona. Both the O VII and Ne IX triplets have been studied for quiescent emission and flares (e.g., Acton et al. 1972; Keenan et al. 1987). In solar flares, the Ne IX lines appeared blended. McKenzie (1985) and Doyle & Keenan (1986) suggested several candidate lines for these blends.

Generally, stars with lower temperature coronae do not show significant blending around the Ne IX triplet. Procyon (Ness et al. 2002b) is a good example. In hotter coronae, the blending is more problematic. To date, the R-ratios measured from Medium Energy Grating (MEG) spectra of Capella have not been used to determine densities (Phillips et al. 2001; Ayres et al. 2001). Ness et al. (2002a) have attempted to disentangle the blending for the LETGS/HRC-S spectrum of Algol by assuming a priori a G-ratio of 0.8.

2.2. *Comparison among the New Instruments*

The new generation of X-ray telescopes of *XMM-Newton* and *Chandra* has opened new dimensions in sensitivity and resolution. Spectroscopic measurements can be carried out with both instruments using the intrinsic resolution of the CCDs (ACIS, EPIC) and the dispersive instruments for higher resolution. Three gratings are providing data: the RGS on board *XMM-Newton* and the HETGS and LETGS on *Chandra*. The HETGS consists of two sets of gratings with different periods, the High Energy Grating (HEG) and the MEG, which intercept X-rays from the inner and outer mirror shells, respectively, and thus are used concurrently. The RGS and HETGS use the EPIC and ACIS-S CCD detectors, respectively, while the LETGS can use either ACIS-S or the microchannel plate detector HRC-S. Figure 2 shows the effective areas and the wavelength ranges for the grating instruments. While RGS, HEG, and MEG operate in the spectral range $\lesssim$40 Å, LETGS covers a much larger wavelength range from 2 to 175 Å. All the gratings have uniform resolving power for their entire wavelength range.

As can be seen from Figure 2 the large wavelength range covered by LETGS allows the extraction of total fluxes, luminosities, and hardness ratios corresponding to *ROSAT* (5–124 Å) or *Einstein* (3–84 Å). With LETGS all He-like triplets ranging from C V and N VI up to Si XIII can be measured simultaneously. LETGS also obtains $\Delta n = 0$ Fe L-shell lines, including density-sensitive lines of Fe XIX to Fe XXII, previously obtained at 5 times lower spectral resolution with *EUVE*.

Since LETGS cannot sort orders via detector intrinsic energy resolution, integrated fluxes and luminosities are still source-model–dependent. For a $\log T = 6.8$ plasma, the apparent energy flux obtained by dividing counts by the first-order effective area is about 20% larger than the true first-order flux, for which 11 orders are accounted. In this ideal isothermal model, only 80% of the counts are from first order.

An advantage of the HETGS is its very high spectral resolution near 1 keV. In addition, order sorting for the HEG, MEG, and RGS is possible using the energy resolution of the CCD detectors, which is not possible for the LETGS/HRC-S configuration. This allows accurate determination of source-model–independent broadband fluxes and luminosities.

The RGS covers a wavelength range similar to *Einstein* with especially large effective areas above 10 Å (Fig. 2). The spectral resolution of the RGS is comparable to that of LETGS in their region of overlap.

The mirror point-spread function primarily defines the dispersed line profile of the HEG, MEG, and LEG. In the case of the RGS, significant scattering wings also arise from the reflection gratings themselves. Grating period variance, detector pixelization, and aspect reconstruction are additional factors. For Ne IX, the RGS offers the highest sensitivity, even in second dispersion order; MEG and LETGS have larger effective areas than HEG. The spectral resolution of the HEG, however, is the most important factor for a realistic assessment of the effects of blending. Here we explore the diagnostic utility for observations of Ne IX with each instrument.

2.3. *Spectral Models*

Atomic data are fundamental to interpretation of the observed spectra. We compare observations with models produced using the Astrophysical Plasma Emission Code (APEC; Smith et al. 2001), version 1.2.[2] APEC incorporates collisional and radiative rate data appropriate for modeling optically thin plasmas under the conditions of collisional ionization equilibrium. The code solves the level-to-level rate matrix to obtain level populations and produces line emissivities as functions of electron temperature and density. APEC also calculates spectral continuum emission from bremsstrahlung, radiative recombination, and two-photon emission.

We rely on APEC inclusion of the H- and He-like atomic data discussed by Smith et al. (2001), the HULLAC calculations of D. Liedahl for the Fe L-shell ions with additional ***R***-matrix calculations available from CHIANTI, version 2.0 (Landi et al. 1999), and isosequence scaling for Ni L-shell ions. Our models assume the ionization balance of Mazzotta et al. (1998) and the solar-abundance model of Anders & Grevesse (1989). Reference wavelengths are from quantum electrodynamic calculations for H- and He-like ions (Drake 1988; Ericsson 1977) and from laboratory measurements for emission lines of Fe L-shell (Brown et al. 1998, 2002) and Ni L-shell ions (Shirai et al. 2000). Additional L-shell wavelengths are derived from HULLAC energy levels.

Despite significant improvements to spectral modeling over the past several years, the theoretical atomic data in APEC and other plasma models remain largely untested over the broad range of applicable densities and temperatures. The deep observations of three late-type stars (Capella, Procyon, and HR 1099), used for in-flight calibration measurements of the dispersion relation and line-spread functions of the gratings, are also useful for determining the extent of agreement between models and observations and for highlighting issues that might require additional atomic physics work. The accuracy of each rate as well as the completeness of line lists is important to the correct interpretation of spectral diagnostics, especially at lower spectral resolution (e.g., Brickhouse et al. 2000). This work is part of a comprehensive effort known as the "Emission Line Project" to benchmark the atomic data in plasma spectral models (Brickhouse & Drake 2000). Work to date on the Capella HETGS spectra has focused on the identification of strong lines for which HEG and MEG give good agreement (e.g., Behar, Cottam, & Kahn 2001; Ayres et al. 2001; Canizares et al. 2000), while we aim to identify weak lines and test a comprehensive model.

Atomic data for the He-like diagnostic lines themselves are exceptionally good; many rates have been benchmarked in controlled laboratory experiments. Tokamak data confirm the calculation of the Ne IX *R*-ratio (Coffey et al. 1994). The transition probability for the forbidden line, which determines the density sensitivity of the Ne IX *R*-ratio, has been measured to 1% accuracy on an electron beam ion trap (EBIT; Wargelin, Beiersdorfer, & Kahn 1993); it has also been confirmed by Bragg crystal spectrometer measurements on the EBIT (Wargelin 1993). Smith et al. (2001) showed that the largest systematic uncertainties in the theory for O VII come from the limited number of energy levels used in calculating the cascades following dielectronic recombination.

APEC models for Ne IX lines are in good agreement with the laboratory measurements. Simplifying assumptions often found in the literature, such as the lack of temperature sensitivity in the *R*-ratio, are no longer necessary since the APEC models are calculated over dense temperature and density grids.

For weak diagnostic lines such as the Ne IX intercombination line, two challenging line measurement issues—determining the continuum level and assessing line blending—are greatly aided by APEC. The APEC line list includes approximately 40 lines with reference wavelengths between 13.35 and 13.85 Å. Furthermore, the APEC emissivity table contains ~1000 lines in that region, down to 4 orders of magnitude weaker than the strong resonance line of Ne IX. This list includes Ne IX dielectronic recombination satellite lines and Fe and Ni L-shell lines with principal quantum number $n \leq 5$. APEC is sufficiently complete over the HETGS bandpass that it can be used to select line-free spectral regions for continuum fitting.

3. OBSERVATIONS AND DATA REDUCTION

Our approach is to use the six observations of HEG calibration data of Capella to obtain a very long total exposure time (154.685 ks) and benchmark the APEC models in the wavelength region around 13.6 Å. The Capella observations discussed in this paper are summarized in Tables 1–3. For each of the three grating instruments, the data from several observations have been combined to produce high signal-to-noise ratio spectra. Standard pipeline processing for HETGS, LETGS, and RGS are described in Canizares et al. (2000), Brinkman et al. (2001), and Audard et al. (2001), respectively.

The HETGS/ACIS-S data were obtained from the *Chandra* archive and reprocessed with CIAO software, version 2.2,[3] and calibration database CALDB, version 2.10.

[2] Available at http://cxc.harvard.edu/atomdb.

[3] Available at http://cxc.harvard.edu/ciao.

TABLE 1
LIST OF *Chandra* HETGS OBSERVATIONS

ObsID	Exposure Time (ks)	Counts[a] HEG	Counts[a] MEG	Observation Start	Observation End	$\log L_X$[b] (ergs s^{-1}) HEG	$\log L_X$[b] (ergs s^{-1}) MEG
00057	28.827	11714	47549	2000 Mar 3, 16:28:53	2000 Mar 4, 01:18:03	30.10	30.19
01010	29.541	10773	42907	2001 Feb 11, 12:22:49	2001 Feb 11, 21:20:17	30.06	30.12
01099	14.565	5934	23634	1999 Aug 28, 07:53:17	1999 Aug 28, 12:16:37	30.12	30.20
01103	40.479	18109	73303	1999 Sep 24, 06:09:21	1999 Sep 24, 18:22:56	30.16	30.24
01235	14.571	5916	24177	1999 Aug 28, 12:16:37	1999 Aug 28, 16:39:57	30.12	30.21
01318	26.701	11133	46338	1999 Sep 25, 13:26:39	1999 Sep 25, 21:51:17	30.14	30.22
Sum.....	154.685	63579	257908	...	...	30.12	30.20

[a] Counts are background-subtracted values. The two dispersion directions are co-added.
[b] The value of L_X was determined within the wavelength range 3–20 Å.

The standard technique for separating the different grating orders employs a variable-width CCD pulse-height filter,[4] which follows the pulse-height versus wavelength relation for each spectral order. Since some observations were made during times of uncertain or changing detector response (primarily CCD temperature changes that affected the gain), the standard filter regions did not trace the actual distributions of events in the pulse-height–wavelength plane very accurately. To mitigate this, we used the constant fractional energy width option available in the CIAO event-resolution program (*tg_resolve_events*) with a fractional width of 0.3. The constant width region accepts more interorder background, particularly at short wavelengths, but this is negligible for our purposes because of the very low background level. We have also bypassed the step of position randomization of events detected within a given pixel, which is part of the standard image processing of ACIS-S. Otherwise, we use the standard CIAO pipeline extraction. We use only the first dispersion orders. The effective areas for positive and negative first orders have been computed for each data set using observation-specific data to account for aspect and bad pixels. The HEG effective areas for the individual observations in the wavelength range around 13 Å are shown in Figure 3, along with the exposure-weighted average effective area to be used for analysis of the combined spectra.

[4] Encoded in the calibration database as the Order Sorting and Integrated Probability file.

The LETGS observations and data reduction are described in Ness et al. (2001). They consist of nine data sets added with a total exposure time of 218.54 ks. Effective areas are from 2001 February (see Pease et al. 2000 for a preliminary description). The RGS observations were taken on 2000 March 25, with an exposure time of 52.92 ks. Data processing is described in Audard et al. (2003). Effective areas have been calculated for the observations with SAS, version 5.3.

We derive X-ray luminosities given in Tables 1–3 of $L_X = 1.3 \times 10^{30}$, 2.8×10^{30}, and 1.7×10^{30} ergs s^{-1}, using the distance of 12.94 ± 0.15 pc (Perryman et al. 1997). Differences are consistent with the different passbands and responses of the instruments. Tables 1 and 2 also show that the luminosities for HETGS and LETGS are fairly constant with time (for HETGS over 1.5 yr), supporting our comparison of spectra taken with different instruments at different times.

4. DATA ANALYSIS

4.1. *Line Flux Measurements*

Table 4 lists 18 strong emission-line features measured in the plus and minus first-order HEG spectra between 13.35 and 13.85 Å, including several features not previously reported for Capella. Line counts are measured with the CORA line-fitting tool developed by Ness et al. (2001) and

TABLE 2
LIST OF *Chandra* LETGS OBSERVATIONS

ObsID	Exposure Time (ks)	Counts (LEG)[a]	Observation Start	Observation End	$\log L_X$ (LEG)[b] (ergs s^{-1})
01167	15.36	41215	1999 Sep 9, 13:10:06	1999 Sep 9, 17:26:08	30.45
01244	12.37	32981	1999 Sep 9, 17:42:27	1999 Sep 9, 21:08:36	30.45
01246	15.00	41701	1999 Sep 10, 03:06:06	1999 Sep 10, 07:16:08	30.47
01248	85.36	240047	1999 Nov 9, 13:42:24	1999 Nov 10, 13:25:05	30.43
01420	30.30	83533	1999 Oct 29, 22:49:29	1999 Oct 30, 07:14:27	30.44
62410	11.33	31491	1999 Sep 9, 23:43:57	1999 Sep 10, 02:52:48	30.48
62422	11.68	31202	1999 Sep 12, 18:26:42	1999 Sep 12, 21:41:20	30.46
62423	14.80	39328	1999 Sep 12, 23:37:44	1999 Sep 13, 03:44:28	30.45
62435	22.34	58201	1999 Sep 6, 00:35:40	1999 Sep 6, 06:48:01	30.42
Sum.....	218.54	599699	...	...	30.41

[a] Counts are background-subtracted values. The two dispersion directions are co-added.
[b] The value of L_X was determined within the wavelength range 3–20 Å. Higher order photons are included without correction.

TABLE 3
List of *XMM-Newton* Observations

ObsID	Exposure Time (ks)	Counts[a] RGS1	Counts[a] RGS2	Observation Start	Observation End	log L_X[b] (ergs s^{-1}) RGS1	log L_X[b] (ergs s^{-1}) RGS2
0121920101[c]	52.92	169423	186267	2000 Mar 25, 11:36:59	2000 Mar 26, 02:53:49	30.22	30.30
0121920101[d]	52.92	45115	44524	2000 Mar 25, 11:36:59	2000 Mar 26, 02:53:49	30.29	30.15

[a] Counts are background-subtracted values. The two dispersion directions are co-added.
[b] The value of L_X was determined within the wavelength range 3–20 Å.
[c] First order.
[d] Second order.

described and refined by Ness & Wichmann (2002). The raw counts obtained with CORA represent the fitted number of expected counts for a given continuum (plus background), requiring Poissonian statistics to be conserved. Measurement errors are given as 1 σ errors and include statistical errors and correlated errors in the cases of line blends but include no systematic errors from, e.g., the continuum

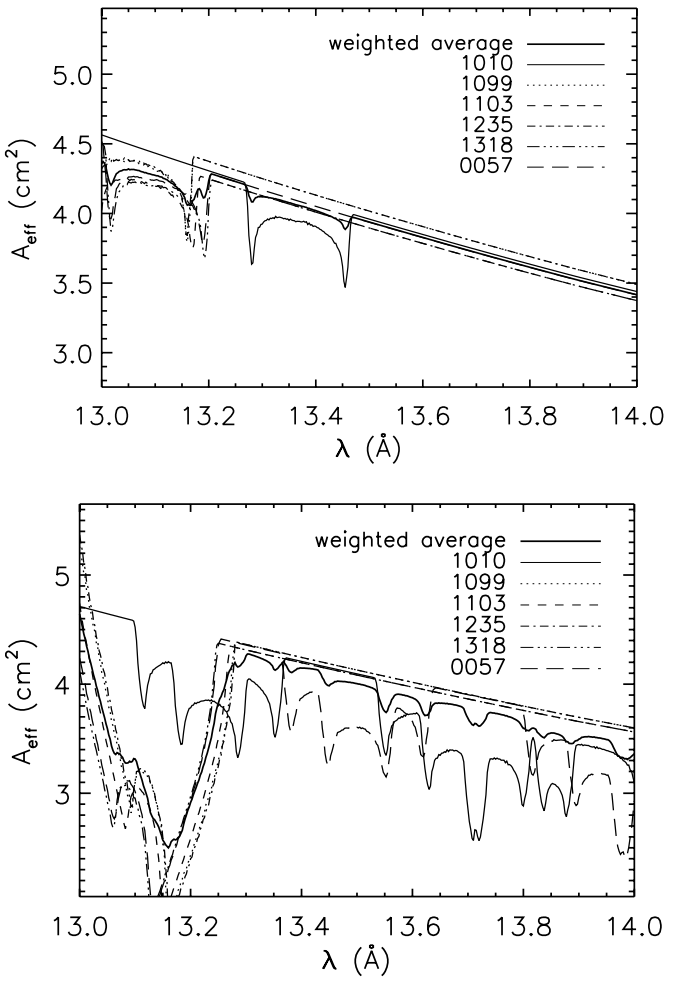

Fig. 3.—Effective areas for the different observations (labeled with observation identification) with the HEG plus first order (*top*) and minus first order (*bottom*). The average is indicated by a thick line and is obtained by weighting with the exposure times. The large dip on the short-wavelength end of the minus first order is the chip gap, while smaller dips are caused by the removal of bad pixels. The widths and shapes of these dips are determined by the aspect dither and the chip geometry.

TABLE 4
Best-Fit Line Fluxes for Separate Dispersion Orders of HEG

λ (Å)	Amplitude[a] (counts)	Flux[b] (photons cm^{-2} ks^{-1})	A_{eff} (cm^2)
	+First Order		
13.449 ± 0.002	315.9 ± 18.4	0.511 ± 0.030	4.00
13.553 ± 0.008	101.7 ± 10.8	0.169 ± 0.018	3.88
13.700 ± 0.004	190.7 ± 14.4	0.331 ± 0.025	3.72
13.358 ± 0.021	31.1 ± 6.4	0.050 ± 0.010	4.07
13.381 ± 0.007	40.6 ± 7.2	0.065 ± 0.012	4.04
13.404 ± 0.007	52.0 ± 8.0	0.084 ± 0.013	3.99
13.427 ± 0.009	64.0 ± 8.7	0.103 ± 0.014	4.01
13.469 ± 0.004	134.8 ± 12.5	0.219 ± 0.020	3.98
13.507 ± 0.002	193.6 ± 15.0	0.318 ± 0.025	3.93
13.524 ± 0.002	316.0 ± 18.7	0.522 ± 0.031	3.91
13.650 ± 0.008	71.2 ± 9.1	0.122 ± 0.016	3.78
13.675 ± 0.009	55.8 ± 8.3	0.096 ± 0.014	3.75
13.722 ± 0.006	54.7 ± 8.2	0.096 ± 0.014	3.70
13.740 ± 0.008	42.2 ± 7.3	0.074 ± 0.013	3.68
13.779 ± 0.004	98.4 ± 10.9	0.175 ± 0.019	3.64
13.797 ± 0.003	146.6 ± 12.9	0.262 ± 0.023	3.62
13.828 ± 0.004	185.8 ± 14.1	0.335 ± 0.025	3.59
13.847 ± 0.007	50.4 ± 8.0	0.091 ± 0.014	3.57
	−First Order		
13.449 ± 0.003	300.6 ± 17.9	0.474 ± 0.028	4.10
13.555 ± 0.006	89.9 ± 10.1	0.148 ± 0.017	3.92
13.700 ± 0.005	182.8 ± 14.0	0.312 ± 0.024	3.78
13.356 ± 0.020	31.1 ± 6.4	0.048 ± 0.010	4.21
13.378 ± 0.007	39.5 ± 7.0	0.061 ± 0.011	4.17
13.404 ± 0.007	60.2 ± 8.4	0.097 ± 0.013	4.02
13.426 ± 0.007	74.8 ± 9.3	0.117 ± 0.015	4.13
13.468 ± 0.004	145.3 ± 12.9	0.236 ± 0.021	3.98
13.507 ± 0.002	204.0 ± 15.7	0.330 ± 0.025	4.00
13.523 ± 0.001	261.7 ± 17.4	0.425 ± 0.028	3.98
13.646 ± 0.007	70.8 ± 9.2	0.119 ± 0.015	3.85
13.673 ± 0.009	42.1 ± 7.4	0.073 ± 0.013	3.75
13.722 ± 0.008	47.7 ± 7.7	0.082 ± 0.013	3.76
13.742 ± 0.008	50.2 ± 7.8	0.089 ± 0.014	3.66
13.778 ± 0.007	94.3 ± 10.5	0.166 ± 0.019	3.67
13.797 ± 0.006	117.1 ± 11.4	0.205 ± 0.020	3.69
13.826 ± 0.003	172.0 ± 13.8	0.313 ± 0.025	3.55
13.843 ± 0.006	55.4 ± 8.5	0.102 ± 0.016	3.50

[a] Measured line counts with 1 σ errors. The line widths are all 0.005 Å, and the assumed continuum level (including background) for each dispersion order is 350 counts Å^{-1}.
[b] The total exposure time was 154.7 ks.

TABLE 5
LINE IDENTIFICATION FOR HEG MEASUREMENTS[a]

λ_{obs}[b] (Å)	λ_{ref}[c] (Å)	λ_{err}[c] (Å)	Ion	Transition	$Flux_{obs}$ (photons cm^{-2} ks^{-1})	$Flux_{model}$[d] (photons cm^{-2} ks^{-1})
13.354	13.355	0.009	Fe XVIII	$2p^5\,{}^2P_{3/2}-2s2p^5({}^3P)3p\,{}^2P_{3/2}$	0.048 ± 0.007	0.0276
13.377	13.385	0.004	Fe XX	$2s2p^4\,{}^4P_{5/2}-2s2p^3({}^5S)3d\,{}^4D_{7/2}$	0.062 ± 0.008	0.0577
	13.390	...	Fe XX	$2p^3\,{}^2P_{3/2}-2p_{1/2}2p_{3/2}3d_{5/2}$	...	0.0046
13.401	13.395	...	Fe XVIII	$2p^5\,{}^2P_{3/2}-2s2p^5({}^3P)3p\,{}^2D_{5/2}$	0.091 ± 0.009	0.0459
	13.407	0.004	Fe XVIII	$2p^5\,{}^2P_{3/2}-2s2p_{1/2}^2 2p_{3/2}^3 3p_{3/2}$	...	0.0238
	13.409	...	Fe XX	$2s2p^4\,{}^4P_{5/2}-2s2p_{1/2}^2 2p_{3/2}3d_{5/2}$	...	0.0169
	13.418	...	Fe XX	$2s2p^4\,{}^4P_{3/2}-2s2p_{1/2}2p_{3/2}^2 3s$	...	0.0108
13.424	13.423	0.004	Fe XIX	$2p^4\,{}^3P_2-2p^3({}^2D)3d\,{}^1F_3$	0.110 ± 0.010	0.0504
	13.431	...	Fe XXI	$2s2p^3\,{}^3S_1-2s2p_{1/2}2p_{3/2}3s$	...	0.0080
	13.432	...	Fe XXI	$2p^3\,{}^2P_{1/2}-2p^2({}^3P)3d\,{}^2P_{3/2}$	...	0.0042
13.446	13.447	0.004	Ne IX	$1s^2\,{}^1S_0-1s2p\,{}^1P_1$	0.492 ± 0.021	0.3978
13.465	13.462	0.003	Fe XIX	$2p^4\,{}^3P_2-2p^3({}^2D)3d\,{}^3S_1$	0.228 ± 0.015	0.1145
13.504	13.497	0.005	Fe XIX	$2p^4\,{}^3P_2-2p_{1/2}2p_{3/2}^2 3d_{3/2}$	0.325 ± 0.018	0.2008
	13.507	0.005	Fe XXI	$2s2p^3\,{}^3D_1-2s2p_{1/2}^2 3s$	...	0.0579
13.521	13.518	0.002	Fe XIX	$2p^4\,{}^3P_2-2p^3({}^2D)3d\,{}^3D_3$	0.471 ± 0.021	0.4425
13.551	13.550	0.005	Ne IX	$1s^2\,{}^1S_0-1s2p\,{}^3P_2$	0.158 ± 0.012	0.0021
	13.551	0.005	Fe XIX	$2p^4\,{}^3P_2-2p_{1/2}2p_{3/2}^2 3d_{5/2}$	...	0.0290
	13.553	0.005	Ne IX	$1s^2\,{}^1S_0-1s2p\,{}^3P_1$	...	0.0531
	13.554	...	Fe XIX	$2p^4\,{}^3P_2-2p_{1/2}^2 2p_{3/2}3d_{5/2}$	...	0.0101
	13.558	...	Fe XX	$2s2p^4\,{}^4P_{1/2}-2s2p_{1/2}^2 2p_{3/2}3d_{3/2}$	...	0.0112
13.645	13.645	0.004	Fe XIX	$2p^4\,{}^3P_2-2p^3({}^2D)3d\,{}^3F_3$	0.118 ± 0.011	0.0712
	13.648	...	Fe XIX	$2p^4\,{}^3P_2-2p^3({}^4S)3d\,{}^3D_3$	...	0.0175
13.671	13.674[e]	...	Fe XIX	$2p^4\,{}^3P_1-2p_{1/2}2p_{3/2}^2 3d_{5/2}$	0.085 ± 0.010	0.0133
	13.675	...	Fe XIX	$2p^4\,{}^3P_1-2p_{1/2}2p_{3/2}^2 3d_{3/2}$	...	0.0264
	13.683	...	Fe XIX	$2p^4\,{}^3P_2-2p_{1/2}2p_{3/2}^2 3d_{3/2}$	...	0.0208
13.697	13.699	0.005	Ne IX	$1s^2\,{}^1S_0-1s2s\,{}^3S_1$	0.322 ± 0.017	0.1845
13.719	13.732[f]	...	Fe XIX	$2p^4\,{}^3P_1-2p_{1/2}2p_{3/2}^2 3d_{5/2}$	0.089 ± 0.010	0.0573
13.738	13.746	...	Fe XIX	$2p^4\,{}^1D_2-2p^3({}^2D)3d\,{}^1F_3$	0.081 ± 0.010	0.0690
13.775	13.767	0.005	Fe XX	$2p^3\,{}^4S_{3/2}-2p^2({}^3P)3s\,{}^4P_{5/2}$	0.170 ± 0.013	0.0494
	13.779	0.005	Ni XIX	$2p^6\,{}^1S_0-2p^5({}^2P)3s\,{}^1P_1$	...	0.0676
13.794	13.795	0.005	Fe XIX	$2p^4\,{}^3P_2-2p_{1/2}2p_{3/2}^2 3d_{5/2}$	0.234 ± 0.015	0.1778
	13.795	0.005	Fe XIX	$2p^4\,{}^1D_2-2p^3({}^2D)3d\,{}^3P_2$	...	0.0207
13.824	13.825	0.002	Fe XVII	$2p^6\,{}^1S_0-2s2p^6 3p\,{}^1P_1$	0.325 ± 0.018	0.3058
	13.839	0.005	Fe XIX	$2p^4\,{}^3P_2-2p_{1/2}^2 2p_{3/2}3d_{5/2}$	...	0.0321
	13.839	0.005	Fe XIX	$2p^4\,{}^1D_2-2p_{1/2}^2 2p_{3/2}3d_{5/2}$	...	0.0082
13.843	13.843	0.006	Fe XX	$2p^3\,{}^4S_{3/2}-2p^2({}^3P)3s\,{}^4P_{3/2}$	0.094 ± 0.011	0.0233

[a] Only the strongest lines modeled are identified. In cases of line blends, weaker lines up to about 10% of the strong line flux are also listed.
[b] Measured HEG wavelengths have been corrected according to the scaling.
[c] Sources for reference wavelengths with errors are given in the text.
[d] Model fluxes are based on the emission measure distribution derived from the lines in Table 6 (shown in Fig. 7).
[e] Brown et al. 2002 list a group of five lines ("O21") with a central wavelength 13.676 ± 0.004, although APEC has not assigned this wavelength to any of the model lines.
[f] APEC includes two relatively strong Ne IX satellite lines that may contribute to a centroid shift.

placement. Line widths are fixed rather than fitted, since line broadening is expected to be predominantly instrumental and line profiles are represented by analytical profile functions (Gaussians for HEG and MEG, Lorentzians for RGS, and for the LETGS modified Lorentzians

$$F(\lambda) = \frac{a}{[1 + (\lambda - \lambda_0)/\Gamma]^{\beta}} ;$$

Kashyap & Drake 2002). The continuum is chosen as an initial guess to be a constant with a level determined by the HEG region at 13.6 Å, which contains no apparent lines in the data as well as no significant emission lines in the APEC database. (The placement of the continuum is discussed further in § 4.3.)

The wavelengths and line counts are listed in Table 4, along with fluxes determined using the total exposure time and effective areas given in the last column for each line. We find the spectra from both dispersion directions to agree reasonably well and use the plus and minus first-order summed spectrum for further analysis (Table 5). The summed spectrum is shown in Figure 4 along with the empirical model, i.e., continuum plus 18 lines, with best-fit centroids and fluxes.

To predict count spectra from the other instruments, we convolved the HEG empirical model with each instrumental response. We allowed global wavelength shifts ($d\lambda$) to account for different absolute dispersion calibrations, and a normalization correction (*Scal*) for differences in effective area calibration. A χ^2 minimization adjusts these two parameters to transform the model to each instrument. Figure 5 shows the MEG and LETGS model and data, while Figure 6 shows RGS1 and RGS2. The instrumental line-spread function width (σ) was not a free parameter, since it is well determined by calibration. The continuum

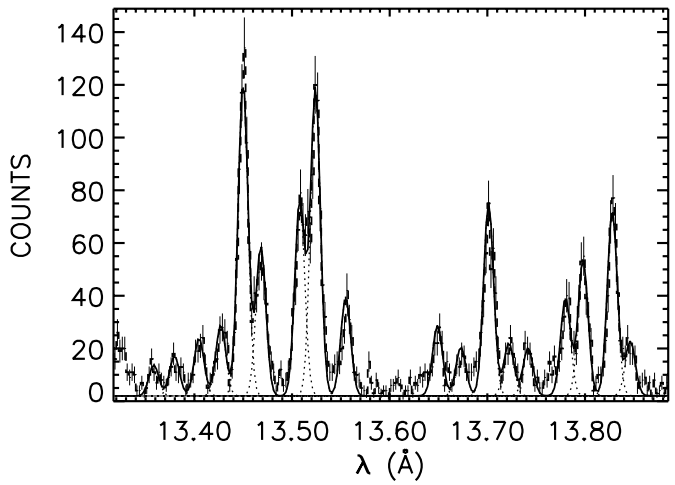

FIG. 4.—HEG summed spectrum of Capella using plus and minus first order. In order to construct an empirical model, 18 emission lines are used with Gaussian line widths $\sigma = 0.005$ Å (equivalent to FWHM = 0.012 Å). The continuum level (including weak lines and background, for combined plus and minus first orders) is chosen constant with 700 counts Å^{-1}. The bin size is 2.5 mÅ, and the exposure time is 154.7 ks.

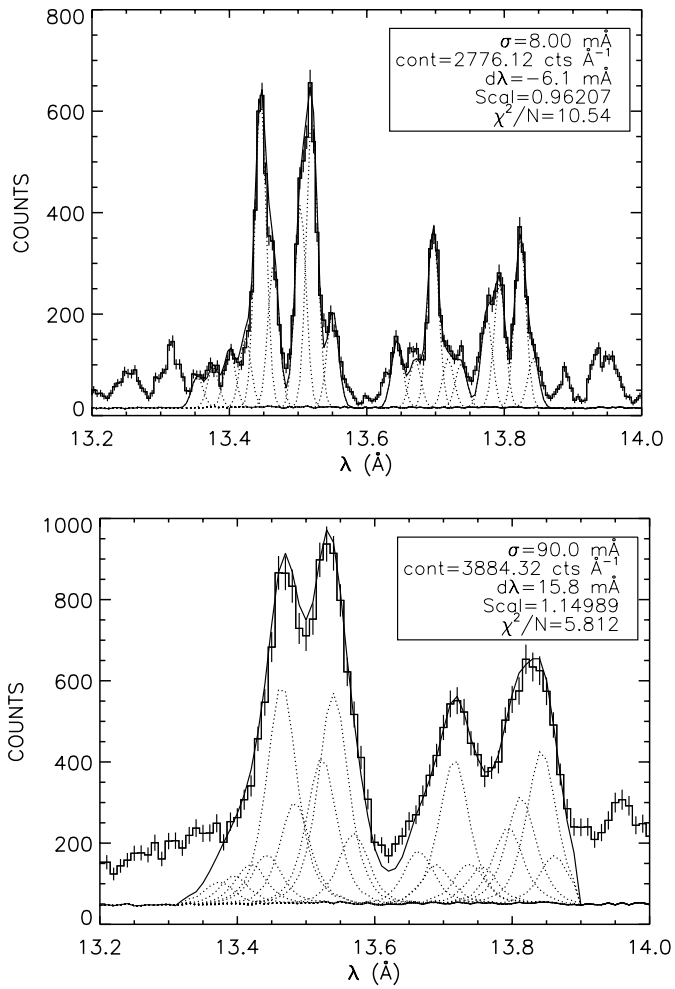

FIG. 5.—Best-fit model obtained from the HEG spectrum, scaled and overlaid on the measured spectra from MEG (*top*) and LETGS (*bottom*). The scaling parameters dλ, *Scal*, σ, and *cont* (described in the text) are listed in the top right inset. The goodness of fit χ^2/N is also given. For MEG the bin size is 5.0 mÅ, and the exposure time is 154.7 ks. For LETGS the bin size is 10.0 mÅ, and the exposure time is 218.5 ks.

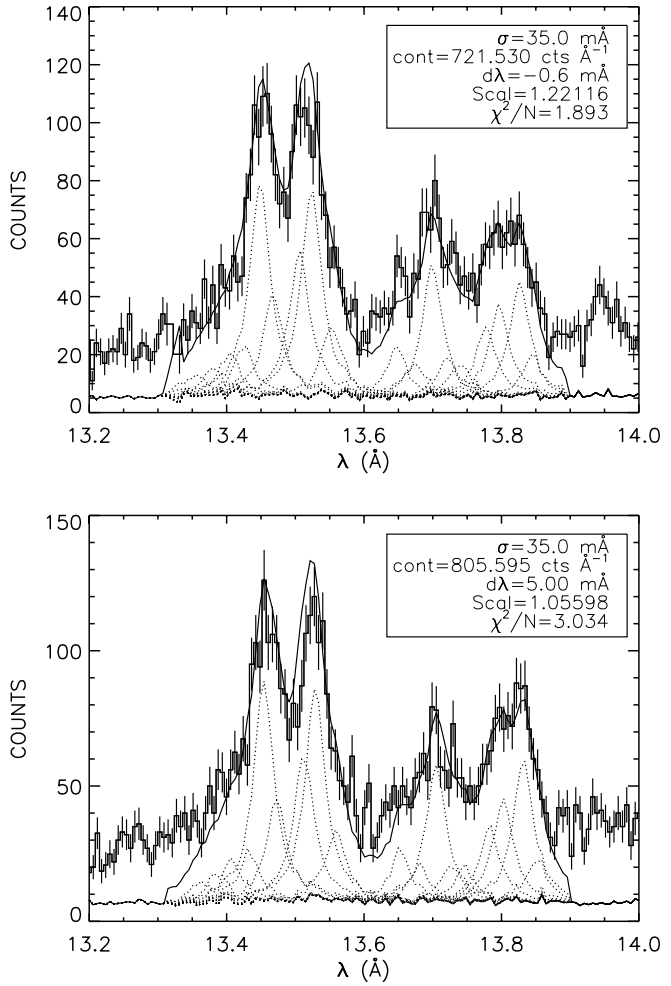

FIG. 6.—Same as Fig. 5, but for RGS1 (*top*) and RGS2 (*bottom*). For RGS1 the bin size is 5.442 mÅ, and for RGS2 the bin size is 6.048 mÅ. The exposure time is 52.92 ks.

(*cont*) was also not a free parameter but was set at the flux level determined from the HEG spectrum. We find excellent agreement between the observed counts and the transformed HEG model, within the systematic errors expected from calibration.

4.2. *Emission Measure Distribution from the HEG Spectrum*

In order to compare our measurements with models we construct a rough emission measure distribution using selected iron lines from ionization stages Fe XV to Fe XXIV (see Table 6). We use the strongest line from each ion (except for Fe XVII) and use other lines to check the model for consistency. The *EUVE* line fluxes are given by Ayres et al. (2001) and are corrected for an interstellar column density $N_{\rm H} = 1.8 \times 10^{18}$ cm^{-2} (Linsky et al. 1993). Assuming collisional ionization equilibrium, we construct an emission measure distribution at low density ($n_e = 1.0$ cm^{-3}) using the APEC line emissivities $\epsilon(T)$. Each emission line specifies an emission measure curve $4\pi d^2(\mathrm{flux_{obs}})/\epsilon(T)$, which represents the emission measure as if each temperature contributed the total emission in the line. It is an upper limit to the final, self-consistent emission measure distribution determined by using the lower envelope of the ensemble of curves as the initial estimate in an iterative optimization

TABLE 6

HEG Iron Line Measurements Useful for Emission Measure Distribution

λ_{obs} (Å)	λ_{ref} (Å)	Ion	Transition	Counts	$Flux_{obs}$ (photons cm^{-2} ks^{-1})	A_{eff} (cm^2)
284.15[a]	284.16	Fe XV	$3s^2\,{}^1S_0-3s3p\,{}^1P_2$	...	10.5[b]	...
335.41[a]	335.41	Fe XVI	$3s\,{}^2S_{1/2}-3p\,{}^2P_{3/2}$	...	33.9[b]	...
15.262[a]	15.261	Fe XVII	$2p^6\,{}^1S_0-2p^5({}^2P)3d\,{}^3D_1$	841.008 ± 29.68	1.128 ± 0.040	4.819
15.015	15.014	Fe XVII	$2p^6\,{}^1S_0-2p^5({}^2P)3d\,{}^1P_1$	2719.34 ± 52.71	3.354 ± 0.065	5.241
17.098	17.096	Fe XVII	$2p^6\,{}^1S_0-2p^5({}^2P)3s\,{}^3P_2$	523.964 ± 22.95	2.459 ± 0.108	1.377
14.207[a]	14.208[c]	Fe XVIII	$2p^5\,{}^2P_{3/2}-2p^4({}^1D)3d\,{}^2D_{5/2}$	1347.92 ± 37.92	1.331 ± 0.037	6.547
	14.208[c]	Fe XVIII	$2p^5\,{}^2P_{3/2}-2p_{1/2}2p_{3/2}^3 3d_{5/2}$			
16.075	16.071	Fe XVIII	$2p^5\,{}^2P_{3/2}-2p^4({}^3P)3s\,{}^4P_{5/2}$	286.749 ± 17.28	0.868 ± 0.052	2.135
14.670[a]	14.664	Fe XIX	$2p^4\,{}^3P_2-2p^3({}^2D)3s\,{}^3D_3$	164.356 ± 14.01	0.190 ± 0.016	5.586
16.110	16.110	Fe XIX	$2s2p^5\,{}^3P_2-2p_{1/2}2p_{3/2}^2 3p_{1/2}$	42.796 ± 7.22	0.136 ± 0.023	2.037
12.847[a]	12.846	Fe XX	$2p^3\,{}^4S_{3/2}-2p_{1/2}2p_{3/2}3d_{3/2}$	372.794 ± 20.84	0.222 ± 0.012	10.875
12.828	12.824	Fe XX	$2p^3\,{}^4S_{3/2}-2p_{1/2}2p_{3/2}3d_{3/2}$	248.643 ± 18.42	0.148 ± 0.011	10.882
	12.827	Fe XX	$2p^3\,{}^4S_{3/2}-2p_{1/2}2p_{3/2}3d_{5/2}$			
	12.822	Fe XXI	$2s2p^3\,{}^3D_1-2s2p_{1/2}2p_{3/2}3d_{5/2}$			
12.286[a]	12.284	Fe XXI	$2p^2\,{}^3P_0-2p3d\,{}^3D_1$	482.550 ± 23.27	0.233 ± 0.011	13.402
11.771[a]	11.770	Fe XXII	$2s^2 2p\,{}^2P_{1/2}-2s^2 3d\,{}^2D_{3/2}$	177.567 ± 14.80	0.077 ± 0.006	14.901
12.750	12.754	Fe XXII	$2s2p^2\,{}^2D_{3/2}-2s2p_{1/2}3s$	90.500 ± 10.40	0.050 ± 0.006	11.610
11.741[a]	11.736	Fe XXIII	$2s2p\,{}^1P_1-2s3d\,{}^1D_2$	107.723 ± 12.10	0.047 ± 0.005	14.666
11.176[a]	11.176	Fe XXIV	$2p\,{}^2P_{3/2}-3d\,{}^2D_{5/2}$	90.073 ± 11.32	0.032 ± 0.004	18.211

[a] This line is used to construct the emission measure distribution.
[b] These measurements are from *EUVE* (Ayres et al. 2001).
[c] Sum of both lines in the blend are used in the model.

to a solution that predicts all measured line fluxes. Figure 7 shows the individual emission measure curves with the best-fit model. The figure also compares an earlier emission measure distribution obtained from simultaneous *EUVE* and *ASCA* observations (Brickhouse et al. 2000).

4.3. *Modeling the Continuum*

Up to this stage of the analysis, the continuum has been taken as a constant value empirically determined from the spectrum. Since the value of the continuum under the weak lines is crucial to the proper derivation of the *R*-ratio (see Brickhouse 2002), we discuss our continuum modeling method in some detail. In this section we derive a formal result that turns out to be close to our initial estimate; in general, iteration to subtract the new continuum flux from lines might be necessary.

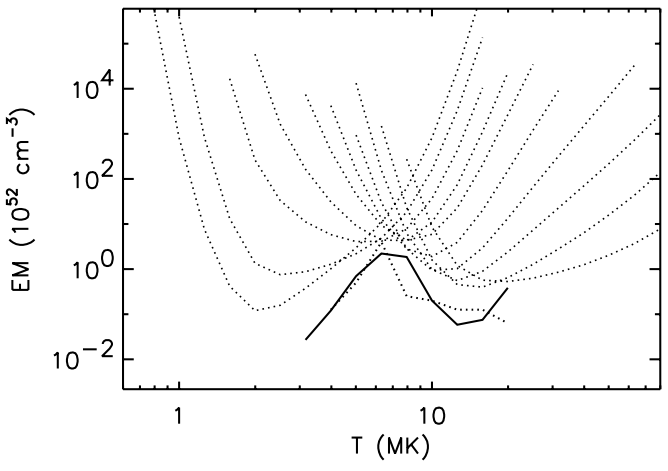

Fig. 7.—Best-fit emission measure distribution derived from iron lines in ionization stages Fe XV to Fe XXIV (*solid line*). The result from Brickhouse et al. (2000) is also shown (*lower dotted line*). Individual line emission measure curves (*upper dotted lines*) are shown for the lines in Table 6.

In principle, background, weak lines, and continuum can be treated separately in the analysis. The background, which includes nonsource events from the detector and cosmic rays, as well as source photons redistributed by mirror scatter, detector aliasing (CCD readout streaking), and grating scatter, is more than a factor of 20 lower than the source-model continuum we derive. The HETGS spectra are not background-subtracted, and so the background is implicitly included in the continuum model. However, the HETGS background rejection is very high: background near 13 Å is estimated[5] to be less than 0.017 counts ks^{-1} $Å^{-1}$ $arcsec^{-1}$, and the extraction width is 5″. Hence, we expect only about 13 counts $Å^{-1}$ per order in the summed HEG spectrum. Weak lines not directly measured (i.e., not listed in Table 5) are treated in § 5.2 as a source of systematic uncertainty to the diagnostic line ratios.

The emission measure distribution constructed in § 4.2 was used to predict both continuum and line fluxes, under the assumption of solar abundances. The tabulated APEC line list includes only lines with emissivities greater than 1.0×10^{-20} photons cm^3 s^{-1}; weaker lines are included as a "pseudocontinuum" and are added to the continuum emission spectrum from bremsstrahlung, radiative recombination, and two-photon emission. The resulting model continuum is flat between 13 and 14 Å and is about 30% lower than the continuum level used in § 4.1 (an initial guess chosen to match at 13.6 Å), a difference of only about 3 counts per emission line.

This model continuum spectrum was then fitted to a set of line-free spectral regions, defined as spectral bins for which the model line flux is less than 20% of the

[5] See the Proposers' Observatory Guide, § 8.3; http://cxc.harvard.edu/proposer/POG.

model continuum flux. Both HEG and MEG were fitted jointly using the Sherpa package in CIAO with the Cash statistic appropriate for low-count bins (Freeman, Doe, & Siemiginowska 2001). With the continuum shape fixed by the emission measure distribution, only a single parameter for the continuum level, or "normalization," was allowed to vary. The resulting fit continuum level was 6% higher than the model continuum level calculated assuming solar abundances. Models with stricter criteria for determining line-free regions give similar results. The continuum level we adopt between 13 and 14 Å thus seems robust.

Since the emission measure distribution was determined only from iron lines, its absolute value should be lowered by 6% to give agreement with the fit continuum level, requiring a 6% higher iron-to-hydrogen abundance ratio. One can draw the preliminary conclusion from this analysis that the iron-to-hydrogen abundance ratio is close to solar; determining accurate abundance ratios requires additional checks from other spectral features and systematic error analysis that is beyond the scope of this paper.

5. RESULTS AND INTERPRETATION

5.1. *Identification of the Emission Lines*

Using our derived emission measure distribution, we predict the spectrum of Capella under the assumptions of solar abundances and low density. We convolve this model spectrum with the instrumental response, allowing only for the small, systematic, global shift in wavelengths, and compare it with the observed HEG spectrum. The model fluxes are given in Table 5 along with the measured fluxes, and the measured spectrum with this model is shown in Figure 8. While the model is calculated at $n_e = 1.0\ \mathrm{cm}^{-3}$, we have used APEC, version 1.3, density-dependent calculations to check the sensitivity of our model iron spectrum. For $n_e < 10^8$ cm^{-3}, no effects larger than a few percent are found. A few weak lines in the model show significant density sensitivity above 10^8 cm^{-3}, but no observable lines show more than 20% change up to $n_e = 10^{13}$ cm^{-3}.

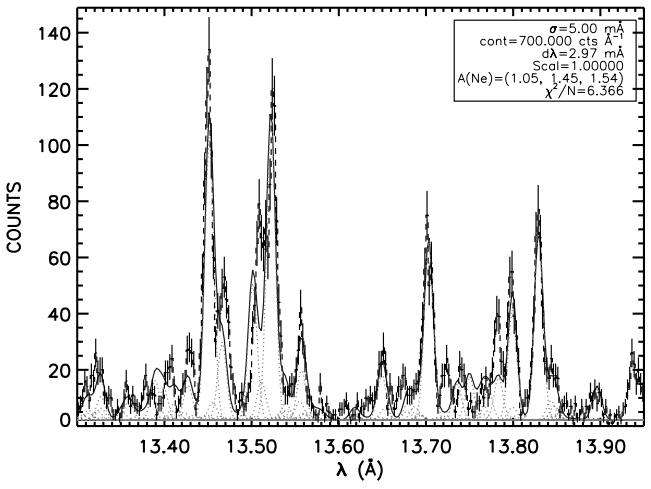

FIG. 8.—Measured spectrum of Capella obtained from HEG (*histogram with error bars*), APEC individual predicted emission lines (*dotted lines*), and their sum (*thick solid line*). Predicted line fluxes were estimated using the emission measure distribution described in § 4.2. Bin size is 2.5 mÅ, and exposure time is 154.7 ks.

Except for one nickel line, only iron and neon lines are present in our model of this spectral region. The most striking discrepancies are seen for the Fe XIX lines at 13.462 Å (flux underpredicted by approximately a factor of 2), at 13.497 Å (flux of blend underestimated by $\sim\frac{1}{3}$; wavelength discrepancy consistent with errors on laboratory wavelengths), and around 13.72–13.75 Å (wavelength discrepancies well within theoretical errors; no laboratory wavelengths available). Minor disagreement is seen around 13.4 Å. The nickel line at 13.779 Å is underpredicted by a factor of 2, probably because of an abundance effect. Since the goal is to assess blending of the neon diagnostic lines, the overall level of agreement is a good indicator of our knowledge of the blending spectrum (especially for Fe XIX). We note that (1) all strong predicted lines are accounted for in the observed spectrum, (2) the worst flux disagreement is a factor of 2, and (3) laboratory iron wavelengths agree with the observations within the errors, while theoretical iron wavelengths appear to agree to within one resolution element of the HEG spectrometer.

Since we have derived the emission measure distribution from iron lines, we can allow the three neon diagnostic line fluxes to vary with independent scaling factors, $A([r, i, f])$, in order to obtain best-fit neon abundances and densities. These parameters are iterated with a χ^2 minimization. After applying the scaling factor $A(r) = 1.03$ for the Ne IX resonance line, we find $\mathrm{flux}_{\mathrm{model}} = 0.41$ photons $\mathrm{cm}^{-2}\,\mathrm{ks}^{-1}$.

The intercombination line (with an adjusted flux of 0.075 photons $\mathrm{cm}^{-2}\,\mathrm{ks}^{-1}$) is significantly weaker in the model than in the observed spectrum. This is, of course, explained by the contaminating lines of Fe XIX and Fe XX that contribute to the observed feature. Table 5 and Figure 9 show that the iron lines can contribute almost half of the total flux measured at 13.55 Å, such that care must be taken with deblending this line, even for HEG spectra. The forbidden line has an adjusted flux of 0.28 photons $\mathrm{cm}^{-2}\,\mathrm{ks}^{-1}$.

5.2. *Treatment of Weak Line Contamination*

Lines that are too weak to be identified and measured in the spectrum (i.e., lines not found in Table 5) are treated as sources of systematic error to the diagnostic line fluxes. The

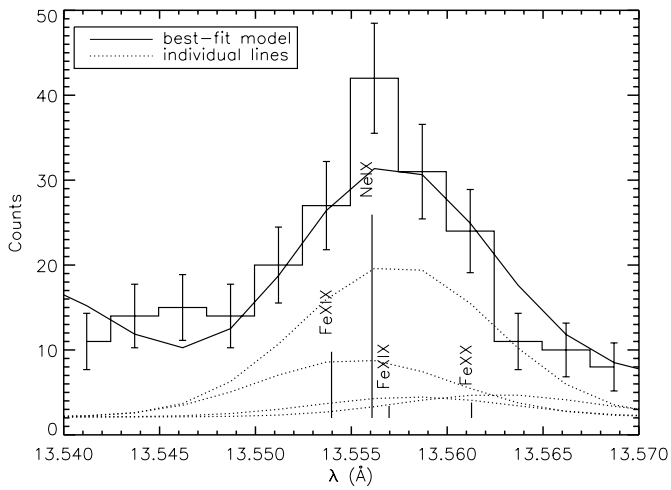

FIG. 9.—Same as Fig. 8, but in more detail, showing the Ne IX intercombination line with contamination.

total weak line flux in the region between 13.35 and 13.85 Å is predicted to be 1.9 times the model continuum flux; however, unlike the flat continuum, this line emission is not randomly distributed. Furthermore, most of the stronger of the unidentified lines have reference wavelengths with small estimated errors. Thus, it is reasonable to compute the fluxes of weak lines within the diagnostic line profile to estimate the degree of contamination. The models indicate that the resonance line contamination is ~5%, while the forbidden and intercombination lines each have ~3% contamination. (This is in addition to the contamination from the 50% blending of the intercombination line, already discussed.)

5.3. *Density and Temperature Diagnostics with* Ne IX *for Capella*

The Ne IX line fluxes constrain electron densities and temperatures. When blends are neglected, the Ne-Fe blended measurement (Table 5) yields an R-ratio of 2.1 ± 0.3, which indicates a density $\log(n_e) = 11.6 \pm 0.1$. Instead, accounting for the blends in the intercombination line based on the emission measure model (see Fig. 9), we derive the low-density limit, $R = 3.95 \pm 0.7$, resulting in $\log(n_e) < 10.2$. Figure 10 shows that the low-density limit is found at all relevant temperatures.

The G-ratio is less affected by blending. The raw measurements result in $G = 0.97 \pm 0.07$, while the deblended fluxes give $G = 0.93 \pm 0.09$, which leads to $T = 2.1 \pm 0.9$ MK (Fig. 11).

The temperature derived from the G-ratio is a factor of 2 lower than the temperature of maximum emissivity (4 MK) but probably consistent given the uncertainties. However, it is inconsistent with expectations based on the emission measure distribution. Figure 12 shows that ~94% of the line emission in our model comes from temperatures above 4 MK. This discrepancy is perhaps most easily interpreted as an abundance effect in an inhomogeneous plasma, although it could also be caused by other effects. Standard emission measure analysis is not valid unless the emitting plasma has uniform abundances; this could easily be incorrect for active binary systems.

If we allow for this possibility in the case of Capella, we could conclude that the dominant 6 MK plasma predicted by the peak in the emission measure distribution must have a lower than solar neon-to-iron ratio. However, if this were the case, in order to preserve the approximately solar neon-to-iron abundance ratio indicated by our line-to-continuum analysis (the scaling factor $A_r = 1.03$ for the Ne IX resonance line), the 2 MK plasma must have a much higher neon-to-iron ratio.

Young et al. (2001) have used the *Far Ultraviolet Spectroscopic Explorer* (*FUSE*) to show that the Fe XVIII emission formed at 6 MK is associated predominantly with the G8 giant, while Johnson et al. (2002), using *HST*/STIS, have

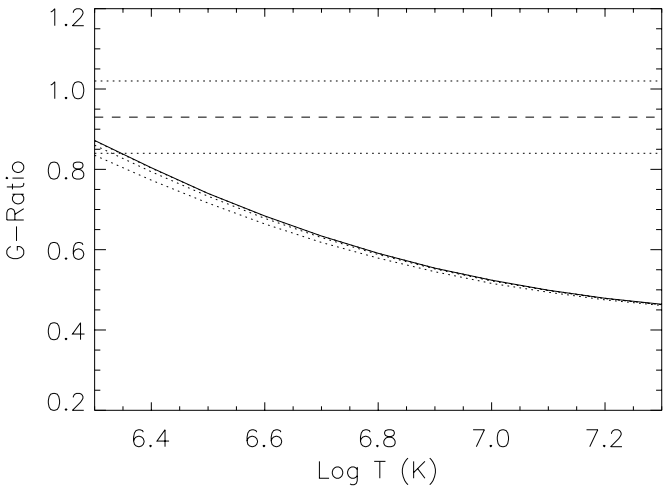

FIG. 11.—Determination of the plasma temperature from the G-ratio for the fluxes adjusted for line blending (*dashed line*). Errors on the measured ratio are represented by dotted lines. APEC models are given for 10^{10}, 10^{11}, 10^{12}, and 10^{13} cm^{-3}, with the solid curve denoting the 10^{10} cm^{-3} (i.e., low-density) model.

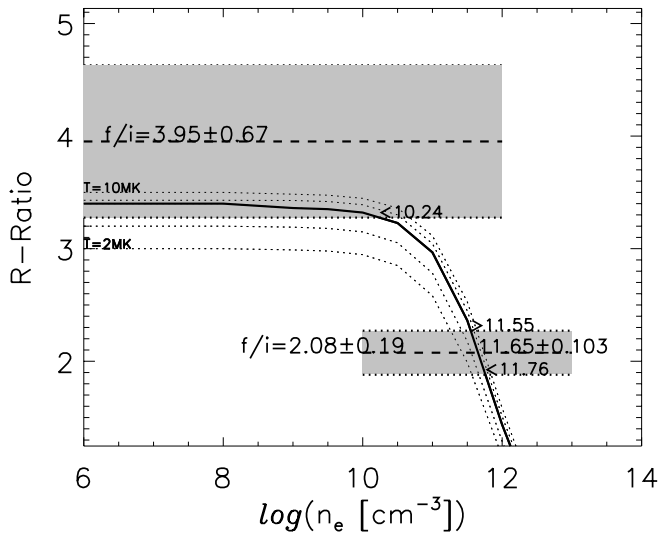

FIG. 10.—Determination of the plasma density from the R-ratio using f and i from the direct measurement ($f/i = 2.1 \pm 0.2$) and from the model accounting for line blends ($f/i = 3.9 \pm 0.7$). Shaded areas represent 1 σ errors on the measured ratios. The upper limit for the density is $\log n_e < 10.2$. APEC models for the density-sensitive curves are shown for $T = 2.0$, 4.0, 6.3, 8.0, and 10 MK, with the curve denoting the 6.3 MK model corresponding to the peak of the emission measure distribution. The R-ratio increases with temperature.

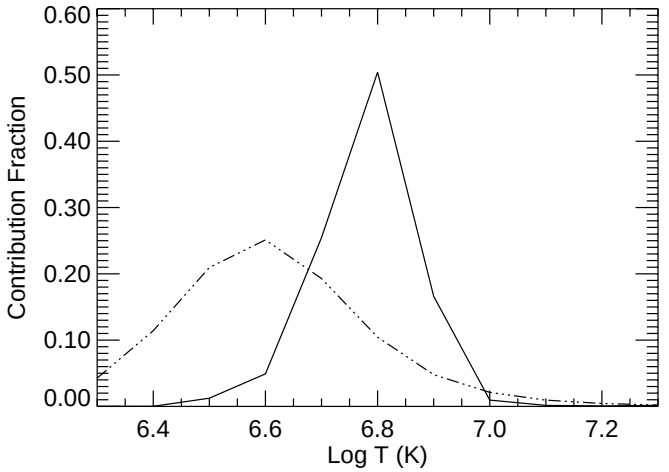

FIG. 12.—Fraction of Ne IX resonance line emission arising from each temperature in the plasma (*solid curve*), derived by multiplying the emission measure distribution of Fig. 7 with the fractional emissivity curve from APEC (*dot-dashed line*). The intercombination and forbidden lines have virtually the same dependences and are not shown.

found Fe XXI emission at ~10 MK to be predominantly on the rapidly rotating G1 giant. These latter observations were concurrent with some of those included in this analysis. Earlier measurements with *HST*/GHRS had found each star contributing roughly half the Fe XXI emission (Linsky et al. 1998).

Our results suggest that a high neon-to-iron abundance ratio is associated with the G1 star. Such a result in the case of the more rapidly rotating star would not be unprecedented. As noted in § 2.1, several analyses of *Chandra* and *XMM-Newton* spectra of active stars indicate abundance ratios for neon to iron considerably in excess of the accepted solar value. Drake et al. (2001) also noted that similar results arose in earlier analyses of low-resolution *ASCA* studies. If the G1 Hertzsprung gap giant has a $3 \times$ solar neon-to-iron ratio in its corona and contributes only 25% at the emission measure distribution peak (based on the *FUSE* Fe XVIII measurement), then the clump giant would need to have less than about 40% of the solar neon-to-iron abundance ratio. A self-consistent analysis is difficult without more stringent constraints on the emission measure distribution, especially below 6 MK. However, although the solar first ionization potential effect presents an existing observational framework for a plausible neon-to-iron ratio significantly below the solar value, it seems coincidental that the abundance ratio of the G8 clump giant would conspire to produce a global average neon-to-iron abundance ratio that agreed so accurately with that of the Sun. Furthermore, preliminary analyses of the clump giants γ Tau (N. S. Brickhouse & A. K. Dupree 2003, in preparation) and β Cet (J. J. Drake et al. 2003, in preparation) do not indicate low neon-to-iron ratios.

While we cannot totally rule out line blending, the required contamination would be far larger than expected. If the *G*-ratio were high because of a contaminated *f*-line, the contaminating line would be the fifth strongest iron line in this region, and therefore difficult for us to have missed. The discrepancy might also arise from errors in the ionization balance. The shape of the emission measure distribution, derived primarily from the ionization balance of iron, is subject to significant atomic data uncertainties (Brickhouse, Raymond, & Smith 1995). One further possible effect concerns the breakdown of the fundamental assumptions implicit in the coronal approximation: that the plasma is optically thin and is in ionization equilibrium. A consistent treatment of the inhomogeneities in the system (two stars with different coronal structures contributing to the emission) is needed in order to test these assumptions. We defer further study of this complicated issue to future work.

For Capella we have used iron lines observed with the HETG and *EUVE* to determine the emission measure distribution. For observations of other stellar coronae, which may have less sampling of the iron ionization stages or lower signal-to-noise ratios than we have for Capella, the construction of an emission measure distribution becomes more complicated. A different approach is suggested (e.g., Schmitt & Ness 2003), in which the emission measure distribution is constructed by use of the H-like Lyα and He-like resonance lines, including a model distribution of magnetic loops.

5.4. *Blending as a Function of Plasma Temperature*

As was noted in § 2.1, the spectra of stellar coronae that are dominated by plasma at significantly lower temperatures than that of Capella show considerably less blending around the Ne IX features, because the populations of the blending ions (primarily Fe XIX) are small. It is of interest to examine this more quantitatively in order to determine the temperature regimes for which Ne IX can be easily used.

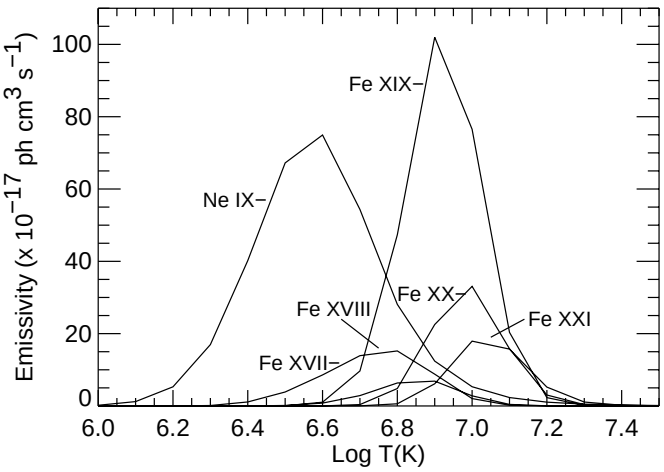

FIG. 13.—Total emissivities as functions of temperature for each ion emitting strong lines in the wavelength range between 13.35 and 13.85 Å. Calculations are APEC models for solar abundances and low density. Table 5 gives the wavelengths for the lines identified in this work.

Figure 13 shows the cooling functions for the neon and blending iron lines. It is apparent that, in plasmas with temperatures $\log T$ below ~6.8, the measurement of Ne IX will not be severely complicated by blending. In plasmas with higher temperatures, the blending will be very strong unless neon is significantly overabundant compared to iron. Large neon-to-iron, as well as neon-to-hydrogen, ratios seem common among active stars, such as in HR 1099 (Brinkman et al. 2001; Drake et al. 2001), II Peg (Huenemoerder et al. 2001), and AR Lac (Huenemoerder et al. 2003). Generally, in all kinds of low-pressure plasmas with high densities but low temperatures, the blending with Fe XIX is less severe, and thus disentangling the Ne IX lines should be fairly straightforward.

6. CONCLUSIONS

The Ne IX triplet is an important tool for estimating plasma densities, not only for coronal plasmas as in Capella, but for plasmas in general in the density range between 10^{10} and 10^{13} cm^{-3}. However, we have shown that the intercombination line of Ne IX is severely blended in plasma with temperatures $\log T \gtrsim 6.8$. This is the case in active coronae as well as in solar flares, such that deblending of high-temperature lines is also important for solar flare diagnostics.

Through our detailed study of Capella spectra, we have found that APEC models are sufficiently accurate and complete that all the significant observed lines in the Ne IX region can be reasonably identified in the HEG spectra. The laboratory wavelengths of Fe XIX from Brown et al. (2002) provide a significant improvement to the accuracy over the wavelengths derived from the HULLAC energy levels. The model fluxes for these lines are also in good agreement with the observations. In the APEC models for Capella, the Ne IX intercombination line is significantly blended. Given the predicted flux of the blending lines, the f/i ratio is consistent with the low-density limit ($n_e < 2 \times 10^{10}$ cm^{-3}).

Interestingly, we find that the temperature-sensitive *G*-ratio is inconsistent with the emission measure distribution derived from iron in the sense that it indicates significantly cooler electron temperatures. Since the strong peak in the emission measure distribution at 6 MK is likely produced predominantly by the G8 star (Young et al. 2001), abundance differences between the two coronae at first seem the most likely explanation for this apparent inconsistency. This would require the neon-to-iron abundance ratio to be lower in the G8 corona than in the G1 corona. In contrast, the neon-to-iron ratio in the G1 corona would have to be higher than solar values such that the average ratio in observations of the Capella system as a whole appear solar.

If correct, this interpretation could have significant implications for coronal analyses in general, since many coronal sources are binary systems comprised of two coronae. Furthermore, if coronae on individual stars are compositionally inhomogeneous (as is the case on the Sun), models will have to account for this. In future work, we will investigate more detailed models to determine what abundance and temperature differences are required to explain the Capella *G*-ratio and emission measure distribution inconsistency. We will also continue the detailed assessment of blending and atomic data for these and other spectra, which may shed further light on this problem.

In the case of Capella spectra obtained by LETGS and RGS, the spectral resolution is inadequate to derive the same results independently from this isolated spectral region. We have not yet explored the possibility of using other stronger, isolated lines from Fe XIX to Fe XXI to specify the iron contribution to the blended Ne IX spectral region and then perform a more constrained fit. The potential problem with this approach is that typical uncertainties in the APEC model line flux ratios ($\sim$20%–30%) may be too large to sufficiently constrain the blending spectrum. With a single test case such as Capella, we cannot explore all the parameter space in the models, and thus any conclusions concerning the treatment of blending cannot yet be generalized. Nevertheless, the good agreement between the APEC models and the HEG observations is encouraging.

We thank Manuel Güdel and Marc Audard for support in reducing the RGS data and Priya Desai for help with the *Chandra* data reduction. We also thank Greg Brown for making the prepublication data from the Lawrence Livermore National Laboratory EBIT available to us. We acknowledge support for J.-U. Ness from NASA LTSA NAG5-3559. J. J. D. and N. S. B. were supported by NASA contract NAS8-39083 to the Smithsonian Astrophysical Observatory (SAO) for the Chandra X-Ray Center (CXC), and D. P. H. was supported by NASA through SAO contract SVI-61010 to the Massachusetts Institute of Technology for the CXC.

REFERENCES

Acton, L. W., Catura, R. C., Meyerott, A. J., & Wolfson, C. J. 1972, Sol. Phys., 26, 183
Anders, E., & Grevesse, N. 1989, Geochim. Cosmochim. Acta, 53, 197
Audard, M., Behar, E., Güdel, M., Raassen, A. J. J., Porquet, D., Mewe, R., Foley, C. R., & Bromage, G. E. 2001, A&A, 365, L329
Audard, M., Güdel, M., Sres, A., Raassen, J. J., & Mewe, R. 2003, A&A, 398, 1137
Ayres, T. R., Brown, A., Osten, R. A., Huenemoerder, D. P., Drake, J. J., Brickhouse, N. S., & Linsky, J. L. 2001, ApJ, 549, 554
Behar, E., Cottam, J., & Kahn, S. M. 2001, ApJ, 548, 966
Blumenthal, G. R., Drake, G. W., & Tucker, W. H. 1972, ApJ, 172, 205
Brickhouse, N. S. 1996, in IAU Colloq. 152, Astrophysics in the Extreme Ultraviolet, ed. S. Bowyer & R. F. Malina (Dordrecht: Kluwer), 105
———. 2002, in ASP Conf. Ser. 277, Stellar Coronae in the *XMM-Newton* and *Chandra* Era, ed. F. Favata & J. J. Drake (San Francisco: ASP), 13
Brickhouse, N. S., & Drake, J. J. 2000, Rev. Mexicana Astron. Astrofis. Ser. Conf., 9, 24
Brickhouse, N. S., Dupree, A. K., Edgar, R. J., Liedahl, D. A., Drake, S. A., White, N. E., & Singh, K. P. 2000, ApJ, 530, 387
Brickhouse, N. S., Raymond, J. C., & Smith, B. W. 1995, ApJS, 97, 551
Brinkman, A. C., et al. 2000, ApJ, 530, L111
———. 2001, A&A, 365, L324
Brown, G. V., Beiersdorfer, P., Liedahl, D. A., Widmann, K., & Kahn, S. M. 1998, ApJ, 502, 1015
Brown, G. V., Beiersdorfer, P., Liedahl, D. A., Widmann, K., Kahn, S. M., & Clothiaux, E. J. 2002, ApJS, 140, 589
Canizares, C. R., et al. 2000, ApJ, 539, L41
Coffey, I. H., Barnsley, R., Keenan, F. P., & Peacock, N. J. 1994, J. Phys. B, 27, 1011
Doyle, J. G., & Keenan, F. P. 1986, A&A, 157, 116
Drake, G. W. 1988, Canadian J. Phys., 66, 586
Drake, J. J. 1996, in ASP Conf. Ser. 109, Cool Stars, Stellar Systems, and the Sun, ed. R. Pallavicini & A. K. Dupree (San Francisco: ASP), 203
Drake, J. J., Brickhouse, N. S., Kashyap, V., Laming, J. M., Huenemoerder, D. P., Smith, R., & Wargelin, B. J. 2001, ApJ, 548, L81
Dupree, A. K., Brickhouse, N. S., Doschek, G. A., Green, J. C., & Raymond, J. C. 1993, ApJ, 418, L41
Ericsson, G. W. 1977, J. Phys. Chem. Ref. Data, 6, 3
Freeman, P., Doe, S., & Siemiginowska, A. 2001, Proc. SPIE, 4477, 76
Gabriel, A. H., & Jordan, C. 1969, MNRAS, 145, 241
Güdel, M., et al. 2001, A&A, 365, L336
Huenemoerder, D. P., Canizares, C. R., Drake, J. J., & Sanz-Forcada, J. 2003, ApJ, 595, 1131
Huenemoerder, D. P., Canizares, C. R., & Schulz, N. S. 2001, ApJ, 559, 1135
Johnson, O., Drake, J. J., Kashyap, V., Brickhouse, N. S., Dupree, A. K., Freeman, P., Young, P. R., & Kriss, G. A. 2002, ApJ, 565, L97
Kashyap, V., & Drake, J. J. 2002, in ASP Conf. Ser. 277, Stellar Coronae in the *XMM-Newton* and *Chandra* Era, ed. F. Favata & J. J. Drake (San Francisco: ASP), 509
Keenan, F. P., McKenzie, D. L., McCann, S. M., & Kingston, A. E. 1987, ApJ, 318, 926
Landi, E., del Zanna, G., Breeveld, E. R., Landini, M., Bromage, B. J. I., & Pike, C. D. 1999, A&AS, 135, 171
Linsky, J. L., Wood, B. E., Brown, A., & Osten, R. A. 1998, ApJ, 492, 767
Linsky, J. L., et al. 1993, ApJ, 402, 694
Mazzotta, P., Mazzitelli, G., Colafrancesco, S., & Vittorio, N. 1998, A&AS, 133, 403
McKenzie, D. L. 1985, ApJ, 296, 294
Mewe, R., Raassen, A. J. J., Drake, J. J., Kaastra, J. S., van der Meer, R. L. J., & Porquet, D. 2001, A&A, 368, 888
Mewe, R., et al. 1982, ApJ, 260, 233
Ness, J.-U., Schmitt, J. H. M. M., Burwitz, V., Mewe, R., & Predehl, P. 2002a, A&A, 387, 1032
Ness, J.-U., Schmitt, J. H. M. M., Burwitz, V., Mewe, R., Raassen, A. J. J., van der Meer, R. L. J., Predehl, P., & Brinkman, A. C. 2002b, A&A, 394, 911
Ness, J.-U., & Wichmann, R. 2002, Astron. Nachr., 323, 129
Ness, J.-U., et al. 2001, A&A, 367, 282
Pease, D. O., et al. 2000, Proc. SPIE, 4012, 700
Perryman, M. A. C., et al. 1997, A&A, 323, L49
Phillips, K. J. H., Mathioudakis, M., Huenemoerder, D. P., Williams, D. R., Phillips, M. E., & Keenan, F. P. 2001, MNRAS, 325, 1500
Pradhan, A. K., & Shull, J. M. 1981, ApJ, 249, 821
Rosner, R., Tucker, W. H., & Vaiana, G. S. 1978, ApJ, 220, 643
Schmitt, J. H. M. M. 1997, A&A, 318, 215
Schmitt, J. H. M. M., Collura, A., Sciortino, S., Vaiana, G. S., Harnden, F. R., Jr., & Rosner, R. 1990, ApJ, 365, 704
Schmitt, J. H. M. M., & Ness, J.-U. 2003, A&A, in press
Schrijver, C. J., Mewe, R., & Walter, F. M. 1984, A&A, 138, 258
Shirai, T., Sugar, J., Musgrove, A., & Wiese, W. L. 2000, J. Phys. Chem. Ref. Data, Monograph 8
Smith, R. K., Brickhouse, N. S., Liedahl, D. A., & Raymond, J. C. 2001, ApJ, 556, L91
Vaiana, G. S., & Rosner, R. 1978, ARA&A, 16, 393
Vedder, P. W., & Canizares, C. R., 1983, ApJ, 270, 666
Wargelin, B. J. 1993, Ph.D. thesis, Univ. California, Berkeley
Wargelin, B. J., Beiersdorfer, P., & Kahn, S. M. 1993, Phys. Rev. Lett., 71, 2196
Young, P. R., Dupree, A. K., Redfield, S., Linsky, J. L., Ake, T. B., & Moos, H. W. 2001, ApJ, 555, L121